



ARTICLE

Characterization of Hydroxyapatite Extracted from Crab Shell Using the Hydrothermal Method with Varying Holding Times

Deni Fajar Fitriyana^{1,2,*}, Rifky Ismail^{1,3,*}, Athanasius Priharyoto Bayuseno¹,
Januar Parlaungan Siregar^{4,5} and Tezara Cionita⁶

¹Department of Mechanical Engineering, Faculty of Engineering, Diponegoro University, Semarang, Jawa Tengah, 50275, Indonesia

²Department of Mechanical Engineering, Faculty of Engineering, Universitas Negeri Semarang, Gunung Pati, Semarang, 50229, Indonesia

³Center for Biomechanics, Biomaterial, Biomechatronics, and Biosignal Processing (CBIOM3s), Diponegoro University, Semarang, 50275, Indonesia

⁴Automotive Engineering Center (AEC), Universiti Malaysia Pahang Al-Sultan Abdullah (UMPSA), Pahang, Malaysia

⁵Faculty of Mechanical & Automotive Engineering Technology, Universiti Malaysia Pahang Al-Sultan Abdullah, Pekan, 26600, Malaysia

⁶Faculty of Engineering and Quantity Surveying, INTI International University, Nilai, Malaysia

*Corresponding Authors: Deni Fajar Fitriyana. Email: deniifa89@mail.unnes.ac.id; Rifky Ismail. Email: rifky_ismail@ft.undip.ac.id

Received: 25 March 2024 Accepted: 29 April 2024

ABSTRACT

Hydroxyapatite (HA) is a bio ceramic commonly utilized in bone tissue engineering due to its bioactive and osteoconductive properties. Crab shells are usually disregarded as waste material despite their significant CaCO_3 content, and have not been widely utilized in the synthesis of HA. This study aims to synthesize and analyze HA derived from crab shells using the hydrothermal method with different durations of holding time. This study utilized precipitated calcium carbonate (PCC) derived from crab shells. With a hydrothermal reactor set at 160°C and varying holding times of 14 (HA_14), 16 (HA_16), and 18 (HA_18) h, a PCC and $(\text{NH}_4)_2\text{HPO}_4$ mixture was used to synthesize HA. The synthesis results were analyzed using scanning electron microscopy (SEM), fourier transform infrared spectroscopy (FTIR), and X-ray diffraction (XRD) tests. This study has accomplished the synthesis of HA from crab shells. Nonetheless, the final product of synthesis still contained CaCO_3 as an impurity. The prolonged hydrothermal holding time of 14 to 18 h resulted in a reduction of impurities while increasing the percentage of crystal weight and crystallite size of HA. Specimen CH_18 is the best-quality product generated in this study. This specimen produced HA with the highest percentage of crystal weight and crystallite size compared to the other specimens. Furthermore, specimen CH_18 exhibited the lowest concentration of impurities. The Ca/P ratio in this specimen was also the closest to 1.67. The Ca/P ratio, crystallite size, and crystal weight percentage of this specimen are 1.54, 19.06 nm, and 99.1%, respectively.

KEYWORDS

Hydroxyapatite; crab shells; CaCO_3 ; hydrothermal; holding time



1 Introduction

Hydroxyapatite (HA), a naturally occurring mineral composed of calcium apatite, has attracted considerable interest in multiple healthcare sectors due to its exceptional biocompatibility, absence of toxicity, and essential role in bone and dental structures. It has found extensive application in biomedical areas such as bone grafting, dental implants, and drug delivery systems [1–3]. Hydroxyapatite is a calcium phosphate that closely resembles the appearance and content of human hard tissues. Specifically, it has a hexagonal and a stoichiometric Ca/P ratio of 1.67, making it exactly the same as bone apatite [4].

Hydroxyapatite, which has the chemical formula $\text{Ca}_{10}(\text{PO}_4)_6(\text{OH})_2$, is commonly used to produce biomaterials to repair and replace hard tissues. Hydroxyapatite is a naturally occurring inorganic component of bone and is extremely compatible with living organisms. Due to its osteoconductive properties, hydroxyapatite is the most often utilized calcium phosphate in orthopedics [5]. In general, hydroxyapatite can be synthesized in several forms, including bulk, microparticles, and nanoparticles. The selection of a form is dependent on the specific application and the desired properties [6]. The bulk hydroxyapatite has a dense three-dimensional arrangement of hydroxyapatite. The bulk hydroxyapatite is widely used in orthopaedic and dental applications such as bone filling, bone grafting, dental implantation, making dental cement, and medical devices coating [7–9]. Hydroxyapatite microparticles have extensive applications in drug delivery systems, biomaterials for bone regeneration, and dental implants [10–13]. Further, hydroxyapatite nanoparticles have been extensively researched for their potential applications in medical fields [14–16]. These include treating osteoporosis, addressing alveolar bone damage in oral surgery, preventing dental caries, repairing minor defects on tooth enamel, and serving as biomaterials in restorative dentistry. In addition, hydroxyapatite nanoparticles possess a substantial surface-to-volume ratio that is highly conducive to usage in drug delivery systems [17–19].

The surging demand for hydroxyapatite can be traced to the exponential growth of the healthcare industry. Furthermore, the growing need for sophisticated materials is fuelling the expansion of the worldwide hydroxyapatite market [20]. Due to its ability to adhere to healthy bone, hydroxyapatite is utilized in orthopedics for joint replacement and bone grafting procedures, improving patient satisfaction. Hydroxyapatite is employed in dentistry to fabricate dental implants, crowns, and bridges due to its inherent similarity to natural teeth [21]. In 2023, the worldwide hydroxyapatite market size amounted to US\$ 2.6 billion. The global hydroxyapatite market is projected to develop at a pace of 5.3% between 2024 and 2032, reaching a value of US\$ 4.2 billion by 2032 [22]. Indonesia has a huge demand for hydroxyapatite for dentistry and orthopedic applications. Due to inadequate domestic production capacity, hydroxyapatite imports have increased. The import value of hydroxyapatite with HS code 28352600 [23] in 2020–2023 totalled US\$ 113,152,629 [24].

Hydroxyapatite can be produced by synthesizing inorganic materials or derived from natural organic-based components. Both biomaterials possess bioactivity and biocompatibility, making them equally suitable for *in vitro* applications. Overall, there are four primary classifications of natural sources that contribute to the synthesis of hydroxyapatite: plant sources, animal sources, biogenic sources, and aquatic sources [25–28].

Biocompatibility is an additional benefit of hydroxyapatite synthesis employing natural materials, in addition to the accessibility of raw materials and the affordability of production [26–28]. Hydroxyapatite derived from natural sources exhibits characteristics that closely resemble those of hydroxyapatite found in the human body. This enhances the potential of hydroxyapatite absorption into human body tissues following medical procedures such as bone grafting or tissue substitution. Thus, using natural materials not only lowers production costs but also reduces the risk of excessive immune reactions or material rejection, boosting the effectiveness and success of hydroxyapatite medicinal applications [26–28].

Indonesia possesses significant potential in the fishing sector, with crab being a routinely exported species to countries such as Japan, the United States, and European nations. The Ministry of Maritime Affairs and Fisheries of the Republic of Indonesia reported that the cumulative export of crab meat between 2019 and 2023 amounted to 144,320 tons [29]. Specifically, the crab comprises 35.77% meat, 51.62% shells, and 12.61% innards [30]. Simultaneously, the quantity of crab shell waste amounted to 208,243 tons, whereas the amount of offal waste totaled 50,871 tons. Inadequate handling of waste generated during crab meat production, such as shells and innards, can lead to pollution and the destruction of the environment [31–33].

According to the above explanation, the quantity of crab shells in Indonesia is substantial and readily accessible. The waste from crab shells holds significant potential for many applications, including producing organic fertilizer [34], chitin [34–36], metal removal from aqueous solutions [35], drug delivery systems [35,37], crackers [38], enhancing calcium content in animal feed [37,39], and chitosan [40,41]. Furthermore, the significant concentration of calcium carbonate (CaCO_3) found in crab shells holds great significance and can serve as a primary substance in biomaterials production, such as hydroxyapatite (HA) [42,43]. Typically, the crab shells consist of between 40% and 70% of calcium carbonate (CaCO_3) [44–46].

To achieve hydroxyapatite of excellent quality, characterized by a stoichiometric Ca/P ratio of 1.67, phase purity, a high level of crystallinity, and a wide range of forms and sizes, it is necessary to exercise precise control over the synthesis process. Hydroxyapatite can be synthesized using hydrolysis, precipitation, sol-gel, and hydrothermal methods. The choice of the synthesis process can influence the material's characteristics, including its topography, morphology, composition, surface properties' non-uniformity, and surface charge of the resultant hydroxyapatite. This will undoubtedly influence its conduct within the human body [47]. Previously, the process of transforming crab shells into hydroxyapatite was conducted using the precipitation method [48–51]. This method was selected because water is the by-product, and the risk of contamination in the synthesis process is minimal. As a result, it can yield highly pure HA with relatively low synthesis costs and a straightforward process [52].

Currently, a total of 969 papers that include both the keywords “shell” AND “hydroxyapatite” have been discovered in the Scopus database from 2015 to 2024. A total of 44 papers were retrieved within the specified time period by employing the combined keywords “crab”, AND “shell”, AND “hydroxyapatite”. However, when the keywords “crab”, AND “shell”, AND “hydrothermal”, AND “hydroxyapatite” was used in the Scopus database search, only 2 papers were discovered.

Hsu et al. [53,54] conducted research on the synthesis of chitosan and hydroxyapatite composites from crab shells using the hydrothermal technique, supplemented with alkali-treated Ti-25Nb-8Sn.

The hydrothermal method is a wet chemical approach that effectively controls the development of complex oxide powders with a high degree of crystallinity [55]. As a result, it has become the preferred method for producing hydroxyapatite nanoparticles. An advantage of this approach, particularly in the manufacture of hydroxyapatite powders, is that it does not create any hydroxyl imperfections in the structure. The hydrothermal process typically operates through chemical reactions in a water-based solution, within a temperature range of 80–400°C and pressure up to 100 KPa, for a significant duration [56]. The hydroxyapatite generated with this technique has a high degree of stoichiometry and a significant crystallinity level. Furthermore, the level of phase purity and the Ca/P ratio substantially increased with the hydrothermal duration and temperature. Because of its excellent biocompatibility, this approach has become the favoured technology for producing hydroxyapatite [55–57]. The hydrothermal method generally involves two stages in forming HA: nucleation and crystal growth. These stages are affected by hydrothermal temperature, hydrothermal time, Ca/P ratio, and pH, which promote the growth of HA crystals [28].

As the previous explanation demonstrates, research on converting CaCO_3 from crab shells into hydroxyapatite by the hydrothermal method has yet to be widely studied. Therefore, this research was conducted to convert CaCO_3 from crab shells into hydroxyapatite by the hydrothermal method. This study aimed to investigate the influence of hydrothermal holding time on the characterization of hydroxyapatite derived from CaCO_3 obtained from crab shells. The hydrothermal process was selected due to its capacity to generate hydroxyapatite crystals of superior quality, greater homogeneity, purity, and yield. Furthermore, this method exhibits cost-effectiveness, minimal energy requirements for dissolving, concise reaction sequences, synthesis conducted at moderate temperatures, and a straightforward methodology [58]. This research is relevant to numerous Sustainable Development Goals (SDGs). In this study, hydroxyapatite extracted from crab shells is characterized to aid in the developing of safer, more effective medical materials that also contribute to improving public health and welfare (SDG 3). Moreover, employing crab shells as a primary material for hydroxyapatite production can serve as a viable approach to minimize waste and promote the sustainable utilization of natural resources, which aligns with Sustainable Development Goal 12. The hydrothermal approach employed serves the dual purpose of enhancing the quality of medical materials (SDG 9) and promoting the preservation of marine ecosystems and the long-term viability of natural resources (SDG 14).

2 Materials and Methods

In this study, the raw material for hydroxyapatite synthesis was precipitated calcium carbonate (PCC) from crab shells produced by the Centre for Bio Mechanics, Bio Materials, Mechatronics, and Bio Signal Processing (CBIOM3S) at Diponegoro University, Semarang, Indonesia. The percentage of C, O, and Ca in PCC are 15.43, 54.44, and 17.56 wt.%, respectively. In addition, the crystal phases contained in PCC are vaterite, aragonite, and calcite, with crystal weight percentages (wt.%) of 98.9, 0.8, and 0.3, respectively [42,43].

The study utilized analytical reagent (AR) grade ammonium hydroxide (NH_4OH) and diammonium hydrogen phosphate ($(\text{NH}_4)_2\text{HPO}_4$) from Merck as the starting materials for the synthesis of hydroxyapatite (HA).

Fig. 1 illustrates the experimental setup. The synthesis of hydroxyapatite (HA) was performed by combining $(\text{NH}_4)_2\text{HPO}_4$ and PCC in a molar ratio of 1.67 Ca/P (3.96 g of $(\text{NH}_4)_2\text{HPO}_4$ and 5 g of PCC), followed by the addition of 25% NH_4OH to achieve a mixture pH of 12. The solution was agitated with a magnetic stirrer for 30 min at a speed of 300 revolutions per minute and a temperature of 30°C [59,60].

The hydroxyapatite synthesis was conducted utilizing the hydrothermal method at a temperature of 160°C , with holding times of 14, 16, and 18 h, respectively. Previous research has indicated that the HA produced by the hydrothermal method at 160°C exhibits high purity, with a minimal impurity content [61,62]. This study's setting up of holding times is based on prior investigations. Previous studies demonstrated the successful synthesis of HA from green mussel shells by hydrothermal methods involving varying holding periods of 14, 16, and 18 h [60]. Moreover, Chen et al. [63] demonstrated that the crystallinity, morphology, and particle size of the hydroxyapatite produced did not undergo any substantial alterations when the reaction time exceeded 18 to 72 h. In this study, the specimen codes of hydrothermal products with holding times of 14, 16, and 18 h are HA_14, HA_16, and HA_18, respectively. Following the final step of the hydrothermal process, the resultant precursor underwent a washing procedure using distilled water and was subsequently filtered with Whatman paper no. 42 until the pH of the filtrate reaches 7. The solid residue was dried in an oven at a temperature of 110°C for 2 h, forming the final product.

Subsequently, the product was assessed by X-ray diffraction (XRD), fourier transform infrared spectroscopy (FTIR), and scanning electron microscopy with energy dispersive X-ray spectroscopy (SEM/EDX) examinations. The crystal structure of hydroxyapatite specimens was characterized using X-ray diffraction (XRD) testing. The investigation involved X-ray diffraction (XRD) testing utilizing a

Shimadzu XRD-7000 machine. The machine was operated at a voltage of 40 kV and a current of 30 mA, and it utilized $\text{CuK}\alpha$ radiation with a wavelength of 1.54056. The experiments were conducted within the angular range of 20° to 80° , with an increment of 0.02° and a scanning rate of 2° per minute. The XRD patterns of the materials acquired from each specimen were analyzed to determine and measure the crystalline phase using HighScore Plus software version 3.0e, which is loaded with the ICDD PDF4 database [64–66]. The software was acquired from PANalytical X'Pert, Cambridge, United Kingdom. Rietveld refinements were conducted using the remaining patterns to assess the accuracy of the refinements. Furthermore, Rietveld refinements were conducted to determine the crystal's weight percentage (wt.%). The diffraction line profiles were described in the Rietveld refinement using the pseudo-Voigt function. This software allows for comparing the sample's diffraction pattern with the reference's diffraction pattern. This software can also be used to determine the crystal orientation and crystal size [67–69].

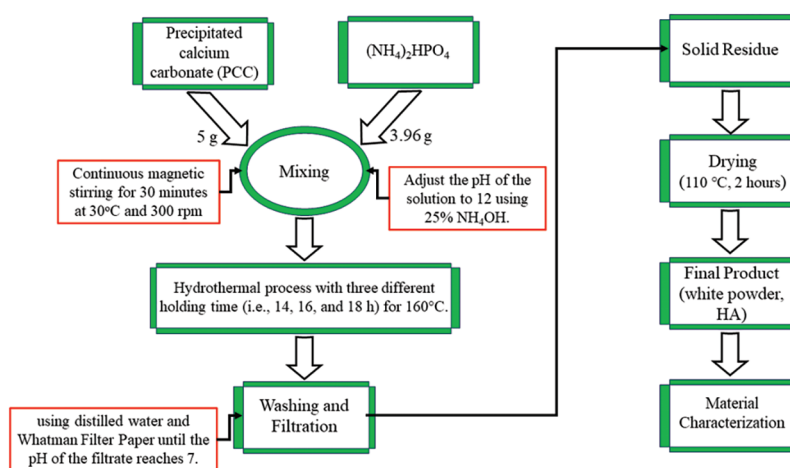


Figure 1: Set-up experiment of hydroxyapatite synthesis

The present study employed Fourier transform infrared (FTIR) analysis to determine the existence and properties of chemical functional groups, including PO_4^{3-} , OH^- , and CO_3^{2-} , in hydroxyapatite samples. A PerkinElmer FTIR spectrometer (CT, USA) was utilized for the FTIR investigation. The FTIR spectra were obtained by measuring wavelengths in the infrared area from 400 to 4000 cm^{-1} . The measurements were taken at 200 scans per second, with a spectral resolution of 2 cm^{-1} [70,71]. Scanning Electron Microscope (SEM) testing was conducted employing a JEOL JSM-6510LA machine (Tokyo, Japan) with an accelerating voltage range of 0.5 to 30 kV to produce morphological pictures of hydroxyapatite. All specimens were coated with gold before the SEM/EDX examination. In addition, an energy-dispersive X-ray (EDX) was employed to ascertain the chemical composition of the surface of each of the hydroxyapatite specimens produced.

3 Results and Discussions

Fig. 2 illustrates the X-ray diffraction (XRD) patterns of each hydroxyapatite (HA) sample generated at different durations of hydrothermal holding time. The two theta values of 10.820 , 16.841 , 22.902 , 25.879 , 28.966 , 31.773 , 32.196 , 32.902 , 34.048 , 39.818 , 43.804 , 43.804 , 46.711 , 48.103 , 49.468 , 50.493 , 51.283 , 52.100 , 53.143 , 55.879 , 61.660 , 64.078 , and 65.031 correspond to the HA peak as indicated by JCPDS card number 09-0432. Nevertheless, the results of this analysis demonstrated that CaCO_3 remained an impurity in all specimens. CaCO_3 is detected by peaks at 2 theta 42.38 , 45.26 , and 61.34 . This demonstrates that not all calcium carbonate (CaCO_3) undergoes a conversion into hydroxyapatite. The

existence of CaCO_3 as an impurity in the resulting synthesized product, along with HA, can be related to the specific crystalline phase of the CaCO_3 utilized in this investigation. The CaCO_3 used in this work primarily comprises the vaterite crystal phase, which forms 98.9% of the crystal weight percentage (wt.%) [42,43].

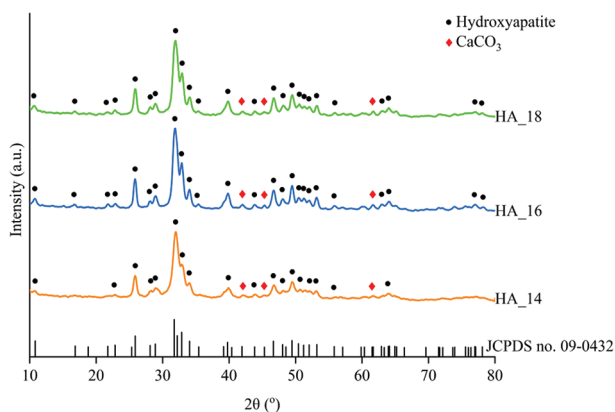


Figure 2: XRD pattern of hydroxyapatite

The hydrothermal procedure will convert aragonite and vaterite minerals into calcite, subsequently transforming hydroxyapatite (HA). Calcite is typically the most stable polymorph of CaCO_3 . In contrast, vaterite and aragonite are CaCO_3 polymorphs that are unstable and metastable [72–75]. The conversion of vaterite crystals into hydroxyapatite (HA) includes the dissolution of vaterite particles, followed by the nucleation and growth of the calcite crystals, which gradually transform into hydroxyapatite. The transformation of vaterite particles into hydroxyapatite occurs at a slow rate. Therefore, the conversion of vaterite to hydroxyapatite may not be fully accomplished, resulting in the presence of CaCO_3 as an impurity [76].

The research conducted by Oral et al. [74] found that the use of a dilute phosphoric acid solution during the conversion of CaCO_3 to HA can cause unstable vaterite particles and metastable aragonite to change into stable calcite particles before transforming into HA. The inadequate holding time duration impedes the successful completion of the conversion process. Consequently, the end product is a hydroxyapatite (HA) structure, with unreacted calcium carbonate (CaCO_3) remaining as an impurity. Sawada et al. [77] found that pure HA cannot be produced by utilizing calcium carbonate with calcite and vaterite crystal phases. This is owing to the fact that amorphous calcium carbonate (ACC) is more soluble than vaterite and calcite. The synthesis of HA is possible with ACC as the precursor. This is due to the increased solubility of ACC. Calcium carbonate solubility is an essential factor in HA precipitation. After calcination, colloidal ACC can precipitate amorphous calcium phosphate (ACP) and yield purified HA or β -TCP. Ca^{2+} are precursors that form the calcium phosphate structure during hydroxyapatite production. In partial or suboptimal reactions, some calcium ions may not be entirely absorbed into the hydroxyapatite structure and remain as calcium carbonate [77]. Various parameters generally influence the purity of HA generated, including temperature, pH, reaction duration, and calcium suspension concentration.

Mahroug et al. [78] found that the concentration of calcium suspension influences the structure and purity of hydroxyapatite. Hydroxyapatite is generated in very concentrated calcium solutions and comprises secondary phases or contaminants and unreacted calcium sources. In contrast, low calcium suspension concentrations encourage the production of hydroxyapatite in the single phase. Previous research has also identified CaCO_3 as a potential impurity in hydroxyapatite production [79–82]. Previous research indicated that HA generated from green mussel shells had the highest purity and no additional impurity phases after an 18-h hydrothermal processing time. At 14 and 16 h, contaminants in CaCO_3 with aragonite crystal phases were still detected [60]. Sirait et al. [79] found that CaO compounds in

hydroxyapatite from broiler eggshells may be attributed to an incomplete dissolution process with phosphoric acid (H_3PO_4). Thus, the hydroxyapatite generated contains CaO, which can absorb CO_2 . This leads to the production of $CaCO_3$ compounds in the final synthesis product.

The specimens were subjected to XRD diffraction analysis using HighScore Plus software for Rietveld analysis (Fig. 3). Fig. 3a presents the Rietveld analysis outcomes for the X-ray diffraction (XRD) pattern of specimen CH_14.

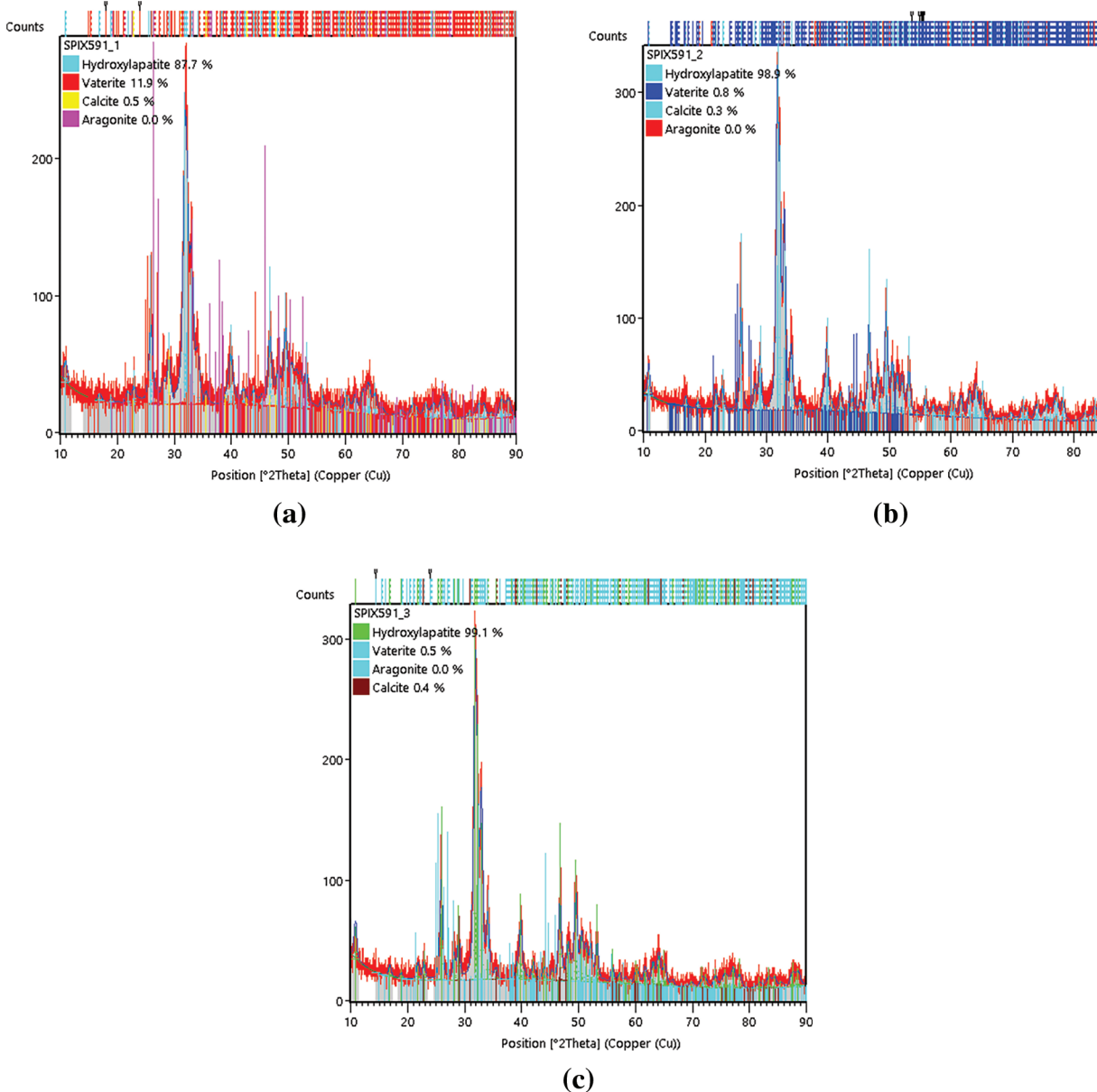


Figure 3: Rietveld analysis on XRD pattern of (a) HA_14, (b) HA_16, and (c) HA_18 specimens

The findings indicated the formation of HA with a hexagonal crystal structure, characterized by lattice parameters of $a = b = 9.41544 \text{ \AA}$ and $c = 6.89952 \text{ \AA}$. In CH_14 specimen, HA crystals' weight percentage and crystallite size were 87.70%, and 11.38 nm, respectively. In addition, the specimen was found to

contain calcite and vaterite, with crystal weight percentages of 0.5% and 11.9%, respectively. The combined amount of CaCO_3 impurities, specifically calcite and vaterite, generated in specimen CH_14 was 12.4%. The crystal structure of HA in specimen CH_16 is hexagonal, with lattice parameters $a = b = 9.42758 \text{ \AA}$ and $c = 6.88825 \text{ \AA}$. The resulting HA compound has a crystal weight percentage of 98.9% and a crystallite size of 16.44 nm. Furthermore, specimen CH_16 generated impurities in the form of CaCO_3 , which comprised calcite and vaterite with respective crystal weight percentages of 0.3% and 0.8% for a total crystal weight percentage of 1.1% (Fig. 3b).

The results of the Rietveld analysis for the X-ray diffraction (XRD) pattern of specimen CH_18 is presented in Fig. 3c. The HA crystal structure in specimen CH_18 is hexagonal, with lattice parameters $a = b = 9.42137 \text{ \AA}$ and $c = 6.88479 \text{ \AA}$. The HA compound obtained has a crystal weight percentage of 99.1% and a crystallite size of 19.06 nm. Additionally, specimen CH_18 produced impurities in the form of CaCO_3 , consisting of calcite and vaterite with crystal weight percentages of 0.4% and 0.5%, respectively, resulting in a total crystal weight percentage of 0.9%. The lattice parameters observed in specimens HA_14, HA_16, and HA_18 exhibit resemblances to the lattice parameters of hydroxyapatite reported in the study conducted by Malau et al. [83]. Their research determined that the lattice parameters of hydroxyapatite (HA) derived from duck egg shells are $a = b = 9.423 \text{ \AA}$ and $c = 6.8801 \text{ \AA}$. Their findings indicated that the generated HA contains identical lattice parameters to commercial HA. The lattice parameters (\AA) obtained in this work are not significantly distinct from the findings of Sadetskaya et al. [84]. The hydrothermal approach was used to create hydroxyapatite nanoparticles, producing a and c of 9.4257 and 6.8875 \AA , respectively. Furthermore, Szterner et al.'s [85] research produced HA for orthopaedic biomaterial applications at different hydrothermal reaction periods, with a and c values ranging from 6.87450–6.88610 \AA and 9.41660–9.43940 \AA , respectively. According to research by Bystrov et al. [86], HA's a and c values are 9.4236 and 6.8802 \AA , respectively. The lattice parameters observed in specimens HA_14, HA_16, and HA_18 show similarities to the hydroxyapatite lattice parameters in JCPDS card number 09-0432 with a and c values of 9.432 and 6.881 \AA , respectively.

Fig. 4 demonstrates the influence of the holding time of the hydrothermal process on both the weight percentage of crystals and the size of crystallites in HA. This finding indicates that extending the hydrothermal holding time from 14 to 18 h results in stronger and sharper HA peaks. This suggests that the level of crystallinity rises proportionally with the holding time duration during the synthesis process [87–89]. Jin et al. [90] also obtained similar findings in their investigation. Their research indicates that as the hydrothermal duration increases, the diffraction peaks become more distinct and integrated, particularly at peak (300). The evidence suggests that the level of crystallinity in HA nanorods is improved as the hydrothermal duration increases [90]. According to findings from a study conducted by Ebrahimi et al. [55], the crystallinity level increased from 82.53% after 4 h of hydrothermal treatment to 86.128% after 10 h.

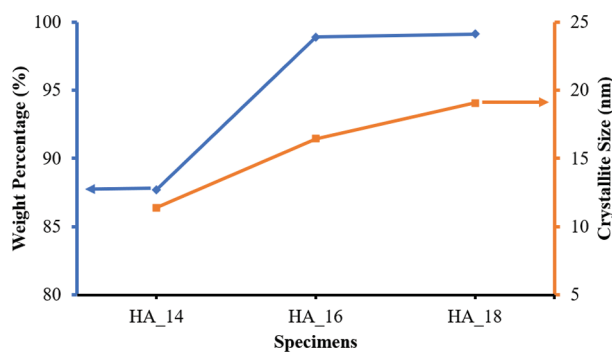


Figure 4: The hydrothermal holding time effect on the crystallite and weight percentage (%) of hydroxyapatite

According to another study by Liang et al. [89], the degree of HA crystallinity increased proportionally to the hydrothermal duration, which increased from two to four hours. The holding time increase used in this investigation increased the weight percentage of HA crystals and caused a reduction in the number of impurities generated. This leads to an enhanced level of HA purity [91]. Furthermore, prolonging the holding time in the hydrothermal process may improve the efficiency of the CaCO₃-to-HA transformation, leading to the formation of larger crystals [92–94]. This is due to the high temperature and pressure conditions that facilitate the hydrothermal process, which aids in the dissolution of CaCO₃ and the formation of HA. Prolonged holding time facilitates the thorough dissolution of CaCO₃, thereby increasing the likelihood of crystal nucleation and subsequent growth, ultimately forming larger HA crystals [95–97]. According to a study by Vu et al. [98], a prolongation of the hydrothermal reaction time to 5 h enabled the synthesized magnetic cellulose nanocrystals to undergo complete conversion of Ag⁺ ions to Ag. Consequently, the peaks of Ag⁺ disappeared while the intensity of the diffraction peaks that define the Ag crystal structure increased. According to an additional investigation by Tian et al. [99], the Nb₂O₅ impurity phase disappeared as the hydrothermal duration was extended. Based on the study conducted by Tang et al. [100], the BiONO₃ impurity peak disappeared as the hydrothermal holding duration increased during the hydrothermal synthesis of Bi₂S₃. An identical result was observed in the study by Shi et al. [101]. As the hydrothermal holding time increased, impurities composed of MnO(OH), MnO(OH)₂-H₂O, and Y(OH)₃ phases disappeared, according to their research. After 24 h of hydrothermal treatment, all impurity phases had entirely disappeared, leaving only the YMn₂O₅ diffraction peak as a single phase.

Fig. 5 displays the results of the Fourier transform infrared spectroscopy (FTIR) test. Calcium carbonate (CaCO₃) identification in PCC can be determined by analyzing the transmission absorption of carbonate ions at the molecular vibrations of the carboxyl bond (O–C) within the range of wave numbers 1600–600 cm⁻¹.

The vibrations can be classified into four main types: symmetric stretching vibrations (ν₁) in the range of 1090–1070 cm⁻¹, out-of-plane bending vibrations (ν₂) in the range of 850–800 cm⁻¹, asymmetric stretching vibrations (ν₃) in the range of 1535–1387 cm⁻¹, and in-plane split bending vibrations (ν₄) in the range of 755–700 cm⁻¹ [102–104].

This study reveals that PCCs derived from crab shells exhibit symmetrical stretching (ν₁), out-of-plane bending (ν₂), asymmetrical stretching (ν₃), and in-plane split bending (ν₄) vibrations at wave numbers of 1086, 877, 1470, and 748 cm⁻¹, respectively. Furthermore, the PCC utilized in this investigation exhibited absorption at 2513 and 3486 cm⁻¹, corresponding to asymmetric stretching vibrations on the C=O functional group and stretching on the O-H functional group, respectively [102–105]. In addition, the FTIR test findings for PCC derived from crab shells revealed peaks at wave numbers 877 and 748 cm⁻¹, which can be attributed to the presence of Ca–O bonds. The peak observed at wave number 1470 cm⁻¹ corresponds to the C–O bond. Previous research by Ismail et al. [106] suggests that the high quantity of CaCO₃ in the sample is associated with Ca–O and C–O in PCC.

The FTIR analysis conducted in this study corroborates the XRD test findings, which have detected the existence of hydroxyapatite (HA) and calcium carbonate (CaCO₃) in the resulting synthesized products. The identification of contaminants in all samples was determined by detecting CO₃²⁻ bending vibrations throughout the range of wave numbers (1/cm) from 1418 to 1460. CO₃²⁻ bending vibrations were detected at wave numbers 1424.23, 1424.01, and 1423.97 (1/cm) in the specimens CH_14, CH_16, and CH_18, respectively. The findings in this study align with the outcomes of research carried out by Sahana et al. [107]. Their FTIR test results also indicated the presence of a peak at a wave number of 1462 (1/cm), which corresponds to the CO₃²⁻ group. According to their findings, CO₃²⁻ indicates that carbon from the organic matter does not undergo complete pyrolysis and instead dissolves into the HA crystal. The FTIR test findings also showed the existence of HA crystals in the produced product.

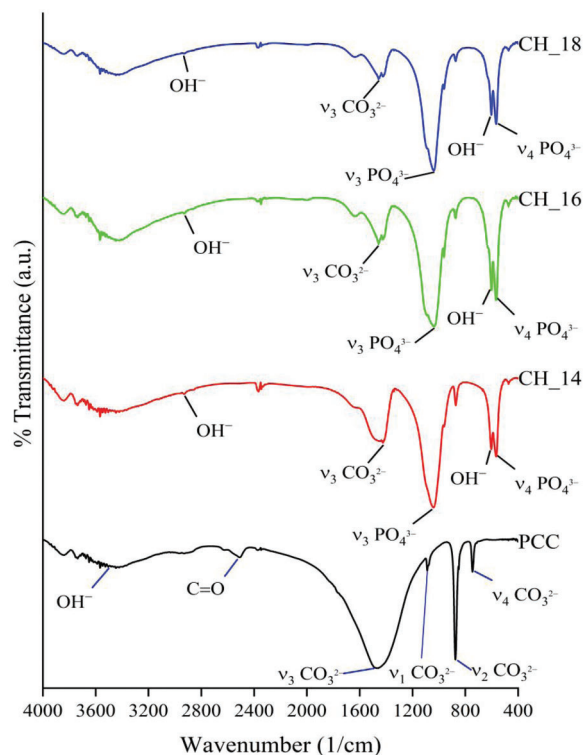


Figure 5: Fourier transform infrared spectroscopy (FTIR) spectra of hydroxyapatite formed

The identification of stretching asymmetry (ν_3) and bending asymmetry (ν_4) in the phosphate group (PO_4^{3-}) and the stretching vibration of the OH group suggests the existence of HA in the synthesized product. The stretching asymmetry of the phosphate group is identified by a peak in the wave number range of 1156–1000 ($1/\text{cm}$). The stretching group phosphate in specimens CH_14, CH_16, and CH_18 is asymmetrical, as indicated by the peaks observed at wave numbers ($1/\text{cm}$) of 1040.02, 1035.37, and 1039.25, respectively. The occurrence of peaks within the wave number range of 600–560 ($1/\text{cm}$) indicates the asymmetrical bending of the phosphate group. The phosphate group in specimens CH_14, CH_16, and CH_18 exhibits bending asymmetry, indicated by peaks at wave numbers ($1/\text{cm}$) of 567.21, 566.64, and 566.95, respectively. Additionally, the stretching vibration of the OH group is observed throughout the wave number range of 3700–2600 ($1/\text{cm}$). The specimens CH_14, CH_16, and CH_18 exhibit a stretching vibration of the OH group, shown by peaks at wave numbers ($1/\text{cm}$) of 3445.71, 3445.42, and 3446.05, respectively.

The findings of this study align with the research carried out by Cursaru et al. [7]. Their Fourier Transform Infrared (FTIR) analysis revealed the presence of PO_4^{3-} and OH groups, which are distinctive features of hydroxyapatite. The stretching vibrations of the OH group and the stretching of the H_2O molecule were seen at wave numbers of 3570 cm^{-1} and $3250\text{--}3500\text{ cm}^{-1}$, respectively. The stretching vibrations of the PO_4^{3-} group were seen at wave numbers ranging from 1095 to 1097 cm^{-1} , 1032 to 1038 cm^{-1} , and 962 cm^{-1} . Furthermore, their synthesis results revealed the presence of CO_3^{2-} groups within the wave number range of $1420\text{--}1489\text{ cm}^{-1}$.

Gritsch et al. [108] conducted FTIR testing on HA and found characteristic bands indicating the presence of phosphate, hydroxyl, and adsorbed water. The analysis identified typical bands at 575 , 610 , 967 , and 1014 cm^{-1} , which indicate the existence of phosphate groups. Additionally, bands at 3568 and 639 cm^{-1} were obtained, indicating the presence of hydroxyl groups. Furthermore, minor amounts of CO_3^{2-} impurities were also detected. Moreover, the results of this investigation exhibit match the research

carried out by Quinaz et al. [109]. FTIR studies were conducted on pure HA as part of their investigation. The test findings indicated the existence of P–O (ν_4) bending vibrations of PO_4^{3-} linked to two distinct bands at around 560 and 600 cm^{-1} . Symmetric and asymmetric P–O (ν_3) stretching modes can be identified based on double splitting bands at about 962 and 1040 cm^{-1} , respectively.

Furthermore, HA exhibited internal hydroxyl stretching vibrations, determined by a visible low peak at around 3550 cm^{-1} .

SEM images of specimens CH_14, CH_16, and CH_18 is shown in Fig. 6. The images in Fig. 6 were taken at a magnification of $2500\times$. Figs. 6a–6c depict the structural characteristics of hydroxyapatite (HA), which was synthesized using the hydrothermal method. The HA generated exhibits an irregular shape in all variations of hydrothermal holding time. Furthermore, the HA particles primarily form agglomerates due to the existence of water molecules that cannot be removed during the sample's drying procedure.

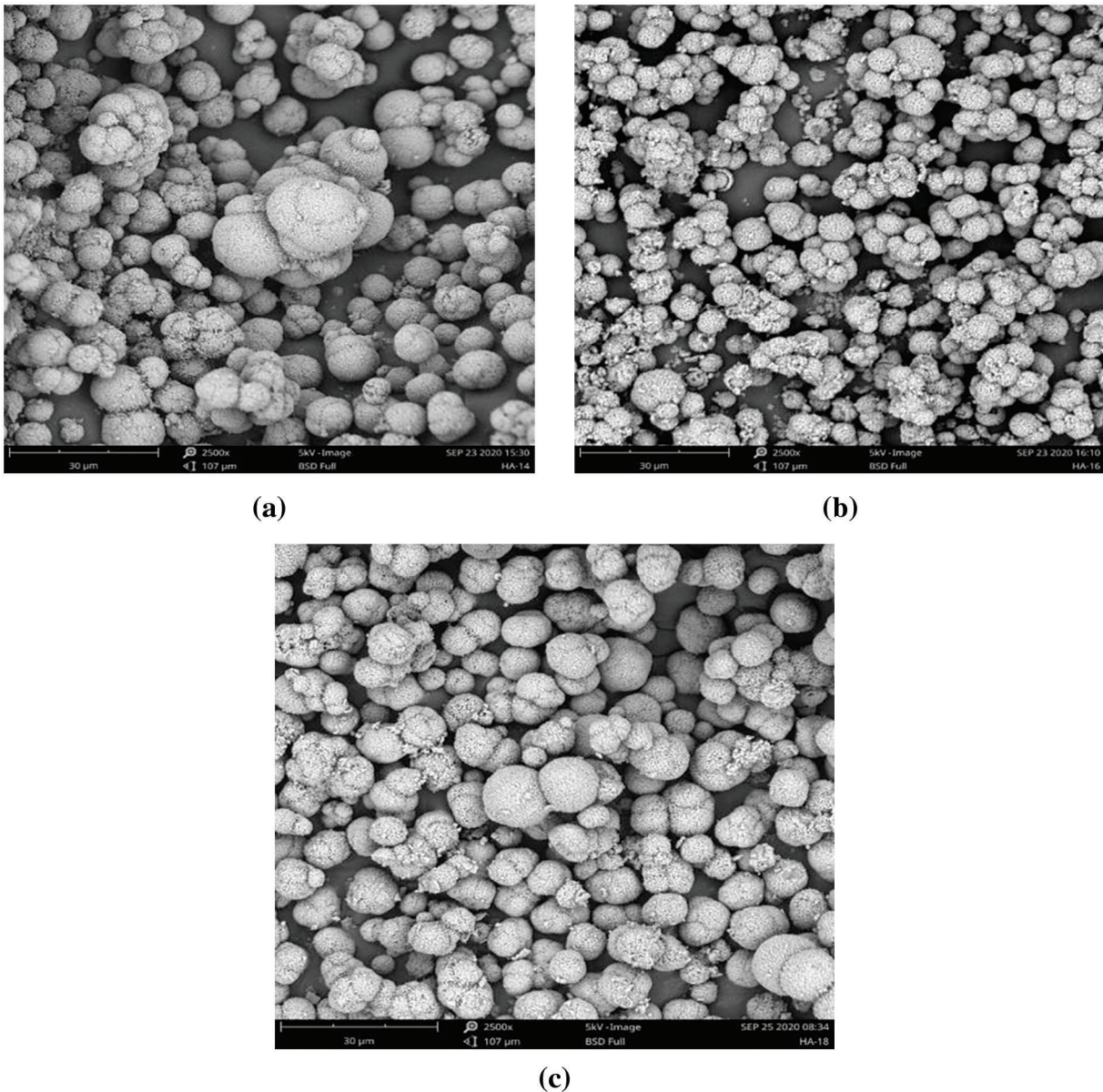


Figure 6: SEM images of (a) CH_14, (b) CH_16, and (c) CH_18 at $2500\times$ magnification

The results of this investigation are comparable to the research carried out by Mohd Pu'ad et al. [110]. The researchers noted that the morphology of hydroxyapatite (HA) obtained from mammalian bones is predominantly characterized by irregular, rod-shaped, flake-shaped, needle-shaped, and flat-like structures. The identical physical form was also discovered in HA derived from aquatic or marine sources. Typically, HA derived from aquatic or marine sources has uneven morphology, including clusters, rods, flakes, needles, and flat-like structures.

The study also concluded that the method or source does not impact the shape variation in the morphology of HA. For instance, employing calcination methods using identical bone sources can yield varying morphologies of hydroxyapatite (HA), including rods, spheres, and needles. The researchers observed that HA derived from mammalian bones exhibited a variety of irregular morphologies, including flakes, needle-like, and slab-like. When HA was created using fish bones and scales, it resulted in various shapes such as flat plates, rod-like structures, irregular shapes, nearly spherical forms, and agglomerates. A study conducted by Sari et al. [111] found that hydroxyapatite (HA) produced from green mussel shells using the precipitation method had a small agglomeration form and a solid structure. The resultant morphology has a granular structure with consistent grain size yet possesses a coarse surface texture. In addition, Obada et al.'s [112] research also yielded HA with various morphologies.

The elemental composition of HA can be verified using EDX data. The findings regarding the elemental composition, specifically the calcium (Ca) and phosphorus (P) content, as well as the calcium-to-phosphorus (Ca/P) molar ratio measurements, are presented in Table 1. The molar ratios of calcium to phosphorus (Ca/P) in the hydroxyapatite (HA) manufactured from crab shells of specimens CH_14, CH_16, and CH_18 was 2.12, 1.89, and 1.54, respectively. The HA generated in this investigation exhibits a Ca/P ratio that exceeds the estimated stoichiometric ratio (1.67), particularly in CH_14 and CH_16. Nevertheless, the Ca/P ratio of CH_18 closely approximates the Ca/P ratio of the pure HA phase.

Table 1: Composition of elements in HA

Specimens	Elements (wt.%)		Ca/P ratio
	Ca	P	
CH_14	11.03	5.21	2.12
CH_16	15.77	8.35	1.89
CH_18	7.14	4.65	1.54

According to the findings of the EDX testing, the synthesis products generated in this study were discovered to have a minor quantity of N as an impurity. The presence of nitrogen (N) in this element results from the synthesis method conducted in this study. The technique involved utilizing PCC derived from crab shells, which contain carbon (C), oxygen (O), calcium (Ca), and nitrogen (N) in the proportions of 15.43%, 54.44%, 17.56%, and 12.57%, respectively. The findings in this study indicate that extending the hydrothermal holding period results in a Ca/P ratio close to 1.67. The findings obtained in this investigation align with the studies conducted by Su et al. [113]. The results of their investigation demonstrated that as the MH heating period increases, the Ca/P ratio gradually approaches 1.67. HA derived from natural sources is typically characterized by a non-stoichiometric nature due to the deviation of the Ca/P ratio from 1.67 [7,26,110]. Ca/P ratios between 1.62 and 2.01 are typical for HA extracted from marine or aquatic sources. The elevated Ca/P ratio observed in HA derived from water or marine sources can be attributed to substituting phosphates within the apatite structure with carbonate

ions (B-type carbonates) [110–112]. Sun et al. [114] also discovered that HA derived from bovine bone and produced via calcination had a Ca/P ratio greater than 1.67.

This is the result of carbonate ion exchange within HA caused by applying calcination techniques. Mardziah et al. [115] conducted research to synthesis HA from eggshells with a Ca/P ratio of 1.71 and demonstrated that HA is a calcium-rich apatite.

4 Conclusions

This research describes the production of hydroxyapatite (HA) from crab shells using the hydrothermal process, with different holding times being tested. An investigation was conducted to explore the holding time's influence on HA powders' physicochemical characteristics. The study revealed that the size of the hydroxyapatite crystals and the percentage of their weight rose with longer hydrothermal holding time. The XRD test findings revealed two theta values corresponding to the HA peak, as indicated by the JCPDS card number 09-0432. Nevertheless, the findings of this investigation indicate that CaCO_3 continues to exist as an impurity in all specimens. This suggests an incomplete conversion of calcium carbonate (CaCO_3) into hydroxyapatite. The holding time increase used in this investigation increased the weight percentage of HA crystals and caused a reduction in the number of impurities generated. This leads to an enhanced level of HA purity. Furthermore, prolonging the holding time in the hydrothermal process may improve the efficiency of the CaCO_3 -to-HA transformation, leading to the formation of larger crystals. The crystal weight percentage of HA obtained in specimens CH_14, CH_16, and CH_18 was 87.7%, 98.9%, and 99.1%, respectively. Additionally, the sizes of the crystallites generated in specimens CH_14, CH_16, and CH_18 are as follows: 11.38, 16.44, and 19.06 nm.

The FTIR analysis conducted in this work corroborates the XRD test findings, which have detected the existence of hydroxyapatite (HA) and calcium carbonate (CaCO_3) in the resulting synthesized products. The identification of contaminants in all samples was determined by detecting CO_3^{2-} bending vibrations throughout the range of wave numbers ($1/\text{cm}$) from 1418 to 1460. The FTIR test findings also showed the existence of HA crystals in the produced product. The identification of stretching asymmetry (ν_3) and bending asymmetry (ν_4) in the phosphate group (PO_4^{3-}) and the stretching vibration of the OH group suggests the existence of HA in the all-synthesized product. The study found that the hydroxyapatite (HA) derived from crab shells exhibited an irregular and agglomerated shape. This morphological form is a prevalent characteristic observed in HA derived from natural substances, particularly those obtained from aquatic or marine origins. The results obtained from this research suggest that as the hydrothermal holding time is prolonged, the Ca/P ratio progressively approaches 1.67. The molar ratios of calcium to phosphorus (Ca/P) in hydroxyapatite (HA) derived from crab shells of specimens CH_14, CH_16, and CH_18 was 2.12, 1.89, and 1.54, respectively. Specimen CH_18 is the best-quality product generated in this study. This specimen produced HA with the highest percentage of crystal weight and crystallite size compared to the other specimens. Furthermore, specimen CH_18 exhibited the lowest concentration of impurities. The calcium-to-phosphorus ratio in this specimen was also the closest to 1.67.

Acknowledgement: The authors express their gratitude to Universitas Diponegoro, Semarang, Indonesia, for the World Class Research (WCR) Grant, which provided the financial support required to conduct this study.

Funding Statement: This study was funded the World Class Research (WCR) Grant of Universitas Diponegoro with Contract Number 357-36/UN7.D2/PP/IV/2024.

Author Contributions: The authors confirm contribution to the paper as follows: study conception and design: Athanasius Priharyoto Bayuseno, Rifky Ismail; data collection: Deni Fajar Fitriyana, Rifky

Ismail; analysis and interpretation of results: Tezara Cionita; draft manuscript preparation: Januar Parlaungan Siregar. All authors reviewed the results and approved the final version of the manuscript.

Availability of Data and Materials: Data available within the article.

Conflicts of Interest: The authors declare that they have no conflicts of interest to report regarding the present study.

References

1. Khalid H, Chaudhry AA. Basics of hydroxyapatite-structure, synthesis, properties, and clinical applications. In: Handbook of ionic substituted hydroxyapatites. Amsterdam: Elsevier Ltd.; 2019. p. 85–115.
2. Mysore THM, Patil AY, Hegde C, Sudeept MA, Kumar R, Soudagar MEM, et al. Apatite insights: from synthesis to biomedical applications. *Eur Polym J.* 2024;209:1–26.
3. Pokhrel S. Hydroxyapatite: Preparation, properties and its biomedical applications. *Adv Chem Eng Sci.* 2018;8(4):225–40. doi:10.4236/aces.2018.84016.
4. Agbeboh NI, Oladele IO, Daramola OO, Adediran AA, Olasukanmi OO, Tanimola MO. Environmentally sustainable processes for the synthesis of hydroxyapatite. *Heliyon.* 2020;6(4):1–13.
5. Bahrololoom ME, Javidi M, Javadpour S, Ma J. Characterisation of natural hydroxyapatite extracted from bovine cortical bone ash. *J Ceram Process Res.* 2009;10(2):129–38.
6. Mohd Pu'ad NAS, Abdul Haq RH, Mohd Noh H, Abdullah HZ, Idris MI, Lee TC. Synthesis method of hydroxyapatite: a review. *Mater Today Proc.* 2020;29:233–9. doi:10.1016/j.matpr.2020.05.536.
7. Cursaru LM, Iota M, Piticescu RM, Tarnita D, Savu SV, Savu ID, et al. Hydroxyapatite from natural sources for medical applications. *Materials.* 2022 Jul;15(15):1–19.
8. Al-Sanabani JS, Madfa AA, Al-Sanabani FA. Application of calcium phosphate materials in dentistry. *Int J Biomater.* 2013;2013:1–12. doi:10.1155/2013/876132.
9. Sopyan I. Preparation of hydroxyapatite powders for medical applications Via Sol-Gel technique. *Indones J Mater Sci.* 2003;4(2):46–51.
10. Feng D, Shi J, Wang X, Zhang L, Cao S. Hollow hybrid hydroxyapatite microparticles with sustained and pH-responsive drug delivery properties. *RSC Adv.* 2013;3(47):24975–82. doi:10.1039/c3ra44609c.
11. Ambrosio JAR, Marmo VLM, Gonçalves EP, Pinto JG, Ferreira-Strixino J, Raniero LJ, et al. Hydroxyapatite microspheres used as a drug delivery system for gliosarcoma strain 9l/Lacz treatment by photodynamic therapy protocols. *Photodiagnosis Photodyn Ther.* 2023;44:1–9.
12. Ameer A, Ali H. A new approach to prepare nano hydroxyapatite from oyster shells used for dental applications. *J Kufa-Phys.* 2019;14(2):1–7.
13. Ashokan A, Kumar TSS, Jayaraman G. Process optimization for the rapid conversion of calcite into hydroxyapatite microspheres for chromatographic applications. *Sci Rep.* 2022;12(1):1–11.
14. Kargozar S, Mollazadeh S, Kermani F, Webster TJ, Nazarnezhad S, Hamzehlou S, et al. Hydroxyapatite nanoparticles for improved cancer theranostics. *J Funct Biomater.* 2022;13(3):1–27.
15. Minaev NV, Minaeva SA, Sherstneva AA, Chernenok TV, Sedova YK, Minaeva ED, et al. Controlled structure of polyester/hydroxyapatite microparticles fabricated via pickering emulsion approach. *Polymers.* 2022;14(20):1–16.
16. Bergara-Muguruza L, Abdelrazik HE, Chen P, Ashida M, Hanawa T, Vallittu P, et al. Calcium carbonate/hydroxyapatite microparticles and osteoblast responses. *Solid State Phenom.* 2022;340:101–6. doi:10.4028/v-09139z.
17. Bonany M, Pérez-Berná AJ, Dučić T, Pereiro E, Martín-Gómez H, Mas-Moruno C, et al. Hydroxyapatite nanoparticles-cell interaction: new approaches to disclose the fate of membrane-bound and internalised nanoparticles. *Biomater Adv.* 2022;142:1–16.

18. Safitri N, Rauf N, Tahir D. Enhancing drug loading and release with hydroxyapatite nanoparticles for efficient drug delivery: a review synthesis methods, surfaceion effects, and clinical prospects. *J Drug Deliv Sci Technol*. 2023;90:1–14.
19. Balhuc S, Campian R, Labunet A, Negucioiu M, Buduru S, Kui A. Review dental applications of systems based on hydroxyapatite nanoparticles—an evidence-based update. *Crystals*. 2021;11(674):1–19.
20. Rial R, González-durruthy M, Liu Z, Ruso JM. Advanced materials based on nanosized hydroxyapatite. *Molecules*. 2021;26(11):1–22.
21. Mishchenko O, Yanovska A, Kosinov O, Maksymov D, Moskalenko R, Ramanavicius A, et al. Synthetic calcium-phosphate materials for bone grafting. *Polymers*. 2023;15(18):1–49.
22. Kaitwade N. Hydroxyapatite market. Available from: <https://www.futuremarketinsights.com/reports/hydroxyapatite-market>. [Accessed 2024].
23. Bahatmaka A. Hydroxyapatite type I. Available from: <https://bmalidi.blogspot.com/2024/06/materials-safety-data-sheet-untuk.html>. [Accessed 2024].
24. Indonesia BS. National export import data. BPS-Statistics Indonesia. Available from: <https://www.bps.go.id/en/exim>. [Accessed 2024].
25. Akram M, Ahmed R, Shakir I, Ibrahim WAW, Hussain R. Extracting hydroxyapatite and its precursors from natural resources. *J Mater Sci*. 2014;49(4):1461–75. doi:10.1007/s10853-013-7864-x.
26. Osuchukwu OA, Salihi A, Abdullahi I, Abdulkareem B, Nwannenna CS. Synthesis techniques, characterization and mechanical properties of natural derived hydroxyapatite scaffolds for bone implants: a review. *SN Appl Sci*. 2021;3(10):1–23.
27. Hammood AS, Hassan SS, Alkhafagy MT, Jaber HL. Effect of calcination temperature on characterization of natural hydroxyapatite prepared from carp fish bones. *SN Appl Sci*. 2019;1(5):1–12.
28. Fitriyana DF, Ismail R, Santosa YI, Nugroho S, Hakim AJ, Syahreza Al Mulqi M. Hydroxyapatite synthesis from clam shell using hydrothermal method: a review. In: *Proceedings of the International Biomedical Instrumentation and Technology Conference (IBITeC)*; 2019; Oct; 23–24. Indonesia; Special Region of Yogyakarta.
29. statistik-kkp. Maritime and fisheries export-import data. The Ministry of Maritime Affairs and Fisheries of the Republic of Indonesia. Available from: <https://statistik.kkp.go.id/home.php?m=eksim&i=211#panel-footer-kpda>. [Accessed 2024].
30. Suwandi R, Nurjanah N, Maharani S. The difference of handling time on weight, proximate composition, and amino acid of steamed crab. *J Pengolah Has Perikan Indones*. 2019;22(1):128–35 (In Indonesian).
31. Islam J, Yap EES, KrongponG L, Toppe J, Peñarubia O. Fish waste management: an assessment of the potential production and utilization of fish silage in Bangladesh, Philippines and Thailand. Rome: *FAO Fisheries and Aquaculture Circular*; 2021.
32. Abdelgalil SA, Abo-Zaid GA. Bioprocess development as a sustainable platform for eco-friendly alkaline phosphatase production: an approach towards crab shells waste management. *Microb Cell Fact*. 2022;21(1):1–36.
33. Venugopal V, Sasidharan A. Seafood industry effluents: environmental hazards, treatment and resource recovery. *J Environ Chem Eng*. 2021;9(2):1–17.
34. Yusuf M, Damayanti LC, Chesidita AD, Sya'di YK. Processing swimming crab shell into value-added products: it utilization as a calcium source flour and flavoring. *Atlantis Press SARL*. 2023;758:189–95.
35. Bhattacharjee BN, Mishra VK, Rai SB, Parkash O, Kumar D. Structure of apatite nanoparticles derived from marine animal (Crab) Shells: an environment-friendly and cost-effective novel approach to recycle seafood waste. *ACS Omega*. 2019;4(7):12753–8. doi:10.1021/acsomega.9b00134.
36. Ngasotter S, Xavier KAM, Meitei MM, Waikhom D, Madhulika, Pathak J, et al. Crustacean shell waste derived chitin and chitin nanomaterials for application in agriculture, food, and health—a review. *Carbohydr Polym Technol Appl*. 2023;6:1–24.
37. Zhang L, Sun P, An X, Wang X, Li S, Lian B. Vaterite synthesized by waste liquid of extracting chitin from crab shells and the mineral loading for doxorubicin hydrochloride. *Minerals*. 2022;12(12):1–17.

38. Yanuar V, Santoso J, Salamah E, Yanuar V, Santoso J, Salamah E, et al. Utilization of crabs shell (*Portunus Pelagicus*) as sources of calcium and phosphorus in making of crackers product. *J Pengolahan Hasil Perikanan*. 2009;12(1):59–72.
39. Muthu M, Gopal J, Chun S, Devadoss AJP, Hasan N, Sivanesan I. Crustacean waste-derived chitosan: antioxidant properties and future perspective. *Antioxidants*. 2021;10(2):1–27.
40. Pakizeh M, Moradi A, Ghassemi T. Chemical extraction and modification of chitin and chitosan from shrimp shells. *Eur Polym J*. 2021;159:1–17.
41. Santos VP, Marques NSS, Maia PCSV, de Lima MAB, de Franco LO, de Campos-Takaki GM. Seafood waste as attractive source of chitin and chitosan production and their applications. *Int J Mol Sci*. 2020;21(12):1–17.
42. Bayuseno AP, Prasetya AI, Ismail R, Setiyana B, Jamari J. Reuse of waste crab shells for synthesis of calcium carbonate as a candidate biomaterial. *Rasayan J Chem*. 2022;15(1):523–8. doi:10.31788/RJC.
43. Ismail R, Cionita T, Shing WL, Fitriyana DF, Siregar JP, Bayuseno AP, et al. Synthesis and characterization of calcium carbonate obtained from green mussel and crab shells as a biomaterials candidate. *Materials*. 2022;15(16):1–15.
44. Ningrum EO, Pratiwi EL, Shaffitri IL, Putra AFP, Karisma AD, Suprpto S. Production of bone implant filaments from blue crab shells (*Portunus pelagicus*) in various synthesis conditions and blending ratios of hydroxyapatite (HAp)-polycaprolactone (PCL). *IOP Conf Ser Earth Environ Sci*. 2022;963(1):1–8.
45. Endang S, Rauf N. Analysis calcium concentration of crab shells on variation of temperature and bioceramic material. *J Phys Conf Ser*. 2019;1242(1):1–4.
46. Suwannasingha N, Kantavong A, Tunkijjanukij S, Aenglong C, Liu H-B, Klaypradit W. Effect of calcination temperature on structure and characteristics of calcium oxide powder derived from marine shell waste. *J Saudi Chem Soc*. 2022;26(2):1–9.
47. Serban A, Teodorescu F, Sofronia AM, Atkinson I, Marinescu CA, Botea-Petcu A, et al. Interplay of the hydroxyapatite structure and morphology with the thermodynamic parameters at hydroxyapatite/protein interface. *Ceram Int*. 2023;49(22):34734–41. doi:10.1016/j.ceramint.2023.08.140.
48. Raya I, Mayasari E, Yahya A, Syahrul M, Latunra AI. Synthesis and characterizations of calcium hydroxyapatite derived from crabs shells (*Portunus pelagicus*) and its potency in safeguard against to dental demineralizations. *Int J Biomater*. 2015;15:1–8.
49. Afriani F, Siswoyo AR, Hudatwi M, Zaitun TY. Hydroxyapatite from natural sources: methods and its characteristics. *IOP Conf Ser Earth Environ Sci*. 2020;599(1):1–7.
50. Rizkayanti Y, Yusuf Y. Optimization of the temperature synthesis of hydroxyapatite from Indonesian crab shells. *Int J Nanoelectron Mater*. 2019;12(1):85–92.
51. Cahyaningrum S, Herdyastuty N, Wiana F, Devina B, Supangat D. Synthesis of hydroxyapatite from crab shell (*Scylla serrata*) waste with different methods added phosphate. *Adv Eng Res*. 2018;171:67–9.
52. Malau ND, Azzahra SF, Guswanto T. Hydroxyapatite preparation from crab shell waste by precipitation method. *Solid State Technol*. 2021;64(3):1–10.
53. Hsu HC, Chung YC, Wu SC, Ho YC, Chang HH, Ho WF. Preparation of chitosan/hydroxyapatite composite coating obtained from crab shells on hierarchical micro/nano-textured Ti surface. *Surf Coatings Technol*. 2022;437:1–8.
54. Hsu HC, Wu SC, Lin CY, Ho WF. Characterization of hydroxyapatite/chitosan composite coating obtained from crab shells on low-modulus Ti-25Nb–8Sn alloy through hydrothermal treatment. *Coatings*. 2023;13:1–12.
55. Ebrahimi S, Nasri CSSM, Bin ASE. Hydrothermal synthesis of hydroxyapatite powders using response surface methodology (RSM). *PLoS One*. 2021;16(5):1–24.
56. Castro MAM, Portela TO, Correa GS, Oliveira MM, Rangel JHG, Rodrigues SF, et al. Synthesis of hydroxyapatite by hydrothermal and microwave irradiation methods from biogenic calcium source varying pH and synthesis time. *Bol Soc Esp Ceram V*. 2022;61(1):35–41. doi:10.1016/j.bsecv.2020.06.003.
57. Irfā'i MA, Schmahl WW, Pusparizkita YM, Muryanto S, Prihanto A, Ismail R, et al. Hydrothermally synthesized-nanoscale carbonated hydroxyapatite with calcium carbonates derived from green mussel shell wastes. *J Mol Struct*. 2024;1306:1–11.

58. Noviyanti AR, Akbar N, Deawati Y, Ernawati EE, Malik YT, Fauzia RP, et al. A novel hydrothermal synthesis of nanohydroxyapatite from eggshell-calcium-oxide precursors. *Heliyon*. 2020;6(4):1–6.
59. Fitriyana DF, Irawan AP, Bahatmaka A, Ismail R, Priharyoto A, Muhamadin RC, et al. The effect of temperature on the hydrothermal synthesis of carbonated apatite from calcium carbonate obtained from green mussels shells. *ARPN J Eng Appl Sci*. 2023;18(11):1215–24.
60. Ismail Rifky, Laroybafih MB, Fitriyana DF, Nugroho Sri, Santoso YI, Hakim AJ, et al. The effect of hydrothermal holding time on the characterization of hydroxyapatite synthesized from green mussel shells. *J Adv Res Fluid Mech Therm Sci*. 2021;80(1):84–93. doi:10.37934/arfmnts.
61. Onoda H, Yamazaki S. Homogenous hydrothermal synthesis of calcium phosphate with calcium carbonate and corbicula shells. *J Asian Ceram Soc*. 2016;4(4):403–6. doi:10.1016/j.jascer.2016.10.001.
62. Jamarun N, Asril A, Zilfa Z, Septiani U. Effect of hydrothermal temperature on synthesis of hydroxyapatite from limestone via hydrothermal method. *Int J Appl Pharm*. 2018;10(1):136–9. doi:10.22159/ijap.2018v10i1.23278.
63. Chen J, Wen Z, Zhong S, Wang Z, Wu J, Zhang Q. Synthesis of hydroxyapatite nanorods from abalone shells via hydrothermal solid-state conversion. *Mater Design*. 2015;87:445–9. doi:10.1016/j.matdes.2015.08.056.
64. Rezvani A, Raji F, Liu Q, Peng Y. Unveiling different pyrrhotite superstructures in copper-gold ore samples: insights from advanced spectroscopic and microscopic characterization. *Miner Eng*. 2024;206:1–12.
65. Hadimani RL. Rare-earth magnetocaloric thin films. In: *Magnetic nanostructured materials: From lab to fab*. Amsterdam: Elsevier Inc.; 2018. p. 269–94.
66. Karim NA, Ramli MM, Ghazali CMR, Mohtar MN. Synthetic graphite production of oil palm trunk chip at various heating rate via pyrolysis process. *Mater Today Proc*. 2019;16:2088–95. doi:10.1016/j.matpr.2019.06.096.
67. Ilmi MM, Nurdini N, Maryanti E, Saiyasombat C, Setiawan P, Kadja GTM, et al. Multi-analytical characterizations of prehistoric rock art pigments from Karim Cave, Sangkulirang-Mangkalihat site, East Kalimantan. *Indonesia Microchem J*. 2020;155:1–8.
68. Triviño-Bolaños DF, Camargo-Amado RJ. Synthesis and characterization of porous structures of rutile $\text{TiO}_2/\text{Na}_{0.8}\text{Ti}_4\text{O}_8/\text{Na}_2\text{Ti}_6\text{O}_{13}$ for biomedical applications. *MethodsX*. 2019;6:1114–23. doi:10.1016/j.mex.2019.04.002.
69. Oh JE, Jun Y, Jeong Y. Characterization of geopolymers from compositionally and physically different Class F fly ashes. *Cem Concr Compos*. 2014;50:16–26. doi:10.1016/j.cemconcomp.2013.10.019.
70. Abifarin JK, Obada DO, Dauda ET, Dodoo-Arhin D. Experimental data on the characterization of hydroxyapatite synthesized from biowastes. *Data Br*. 2019;26:1–8.
71. Vinoth Kumar KC, Jani Subha T, Ahila KG, Ravindran B, Chang SW, Mahmoud AH, et al. Spectral characterization of hydroxyapatite extracted from Black Sumatra and fighting cock bone samples: a comparative analysis. *Saudi J Biol Sci*. 2021;28(1):840–6. doi:10.1016/j.sjbs.2020.11.020.
72. Berdonosov SS, Znamenskaya IV, Melikhov IV. Mechanism of the vaterite-to-calcite phase transition under sonication. *Inorg Mater*. 2005;41(12):1483–7.
73. Unger RE, Stojanovic S, Besch L, Alkildani S, Schröder R, Jung O, et al. *In vivo* biocompatibility investigation of an injectable calcium carbonate (Vaterite) as a bone substitute including compositional analysis via SEM-EDX technology. *Int J Mol Sci*. 2022;23(3):1–16.
74. Oral Ç.M, Çalışkan A, Kapusuz D, Ercan B. Facile control of hydroxyapatite particle morphology by utilization of calcium carbonate templates at room temperature. *Ceram Int*. 2020;46(13):21319–27. doi:10.1016/j.ceramint.2020.05.226.
75. Myszka B, Schübler M, Hurler K, Demmert B, Detsch R, Boccaccini AR, et al. Phase-specific bioactivity and altered Ostwald ripening pathways of calcium carbonate polymorphs in simulated body fluid. *RSC Adv*. 2019;9(32):18232–44. doi:10.1039/C9RA01473J.
76. Schröder R, Pohlit H, Schüller T, Panthöfer M, Unger RE, Frey H, et al. Transformation of vaterite nanoparticles to hydroxycarbonate apatite in a hydrogel scaffold: relevance to bone formation. *J Mater Chem B*. 2015;3(35):7079–89. doi:10.1039/C5TB01032B.

77. Sawada M, Sridhar K, Kanda Y, Yamanaka S. Pure hydroxyapatite synthesis originating from amorphous calcium carbonate. *Sci Rep.* 2021;11(1):1–9.
78. Mahroug H, Mansri A, Dergal F. The effect of calcium suspension concentration on the hydroxyapatite structures and purity. *Rev Roum Chim.* 2019;64(3):277–86. doi:10.33224/rrech.
79. Sirait M, Sinulingga K, Siregar N, Damanik YF. Synthesis and characterization of hydroxyapatite from broiler eggshell. *AIP Conf Proc.* 2020;2221:1063–6.
80. Kamitakahara M, Nagamori T, Yokoi T, Ioku K. Carbonate-containing hydroxyapatite synthesized by the hydrothermal treatment of different calcium carbonates in a phosphate-containing solution. *J Asian Ceram Soc.* 2015;3(3):287–91. doi:10.1016/j.jascr.2015.05.002.
81. Pham Minh D, Rio S, Sharrock P, Sebei H, Lyczko N, Tran ND, et al. Hydroxyapatite starting from calcium carbonate and orthophosphoric acid: synthesis, characterization, and applications. *J Mater Sci.* 2018;49(12):4261–9.
82. Cestari F, Agostinacchio F, Galotta A, Chemello G, Motta A, Sglavo VM. Nano-hydroxyapatite derived from biogenic and bioinspired calcium carbonates: synthesis and *in vitro* bioactivity. *Nanomaterials.* 2021;11(2):1–14.
83. Malau ND, Adinugraha F. Synthesis of hydroxyapatite based duck egg shells using precipitation method. *J Phys Conf Ser.* 2020;1563(1):1–8.
84. Sadetskaya AV, Bobrysheva NP, Osmolowsky MG, Osmolovskaya OM, Voznesenskiy MA. Correlative experimental and theoretical characterization of transition metal doped hydroxyapatite nanoparticles fabricated by hydrothermal method. *Mater Charact.* 2021;173:1–14.
85. Szterner P, Antosik A, Pagacz J, Tymowicz-Grzyb P. Morphology control of hydroxyapatite as a potential reinforcement for orthopedic biomaterials: the hydrothermal process. *Crystals.* 2023;13(5):1–23.
86. Bystrov V, Paramonova E, Avakyan L, Coutinho J, Bulina N. Simulation and computer study of structures and physical properties of hydroxyapatite with various defects. *Nanomaterials.* 2021;11(10):1–30.
87. Rodrigues A, Sena da Fonseca B, Ferreira Pinto AP, Piçarra S, Montemor MF. Synthesis and application of hydroxyapatite nanorods for improving properties of stone consolidants. *Ceram Int.* 2022;48(10):14606–17. doi:10.1016/j.ceramint.2022.02.004.
88. Zhu Y, Xu L, Liu C, Zhang C, Wu N. Nucleation and growth of hydroxyapatite nanocrystals by hydrothermal method. *AIP Adv.* 2018;8(8):1–11.
89. Liang W, Niu Y, Ge S, Song S, Su J, Luo Z. Effects of hydrothermal treatment on the properties of nanoapatite crystals. *Int J Nanomed.* 2012;7:5151–8.
90. Jin X, Chen X, Cheng Y, Wang L, Hu B, Tan J. Effects of hydrothermal temperature and time on hydrothermal synthesis of colloidal hydroxyapatite nanorods in the presence of sodium citrate. *J Colloid Interface Sci.* 2015;450:151–8. doi:10.1016/j.jcis.2015.03.010.
91. Matamoros-Velozza Z, Rendon-Angeles JC, Yanagisawa K, Ueda T, Zhu K, Moreno-Perez B. Preparation of silicon hydroxyapatite nanopowders under microwave-assisted hydrothermal method. *Nanomaterials.* 2021;11(6):1–16.
92. Ruffini A, Sprio S, Preti L, Tampieri A. Synthesis of nanostructured hydroxyapatite via controlled hydrothermal route. In: Barbeck M, Jung O, Smeets R, Koržinskas T, editors. *Biomaterial-supported tissue reconstruction or regeneration.* Rijeka: IntechOpen; 2019. p. 1–22.
93. Earl JS, Wood DJ, Milne SJ. Hydrothermal synthesis of hydroxyapatite. *J Phys Conf Ser.* 2006;26(1):268–71.
94. Du H, Steinacher M, Borca C, Huthwelker T, Murello A, Stellacci F, et al. Amorphous CaCO₃: influence of the formation time on its degree of hydration and stability. *J Am Chem Soc.* 2018;140(43):14289–99. doi:10.1021/jacs.8b08298.
95. Lee SW, Kim YJ, Lee YH, Guim H, Han SM. Behavior and characteristics of amorphous calcium carbonate and calcite using CaCO₃ film synthesis. *Mater Des.* 2016;112:367–73. doi:10.1016/j.matdes.2016.09.099.
96. Seepma SYMH, Ruiz-Hernandez SE, Nehrke G, Soetaert K, Philipse AP, Kuipers BWM, et al. Controlling CaCO₃ particle size with {Ca²⁺};{CO₃²⁻} ratios in aqueous environments. *Cryst Growth.* 2021;21(3):1576–90. doi:10.1021/acs.cgd.0c01403.

97. Stojanović ZS, Ignjatović N, Wu V, Žunić V, Veselinović L, Škapin S, et al. Hydrothermally processed 1D hydroxyapatite: mechanism of formation and biocompatibility studies. *Mater Sci Eng C Mater Biol Appl.* 2016;68:746–57. doi:10.1016/j.msec.2016.06.047.
98. Vu AN, Le HN, Phan TB, Le HV. Facile hydrothermal synthesis of Ag/Fe₃O₄/cellulose nanocomposite as highly active catalyst for 4-nitrophenol and organic dye reduction. *Polymers.* 2023;15(16):1–17.
99. Tian X, Qi Q, Hou B, Qian Y. Hydrothermal synthesis and upconversion luminescence of cubic-shaped LiNbO₃: Yb³⁺/Er³⁺ nanocrystals. *Inorg Chem Commun.* 2023;157:1–9.
100. Tang C, Wang C, Su F, Zang C, Yang Y, Zong Z, et al. Controlled synthesis of urchin-like Bi₂S₃ via hydrothermal method. *Solid State Sci.* 2010;12(8):1352–6. doi:10.1016/j.solidstatesciences.2010.05.007.
101. Shi J, Wang J, He H, Lu Y, Shi Z. Rodlike YMn₂O₅ powders derived from hydrothermal process using oxygen as oxidant. *Materials.* 2020;13(3):1–11.
102. Henggu KU, Ibrahim B, Suptijah P. Hydroxyapatite production from cuttlebone as bone scaffold material preparations. *J Pengolah Has Perikan Indones.* 2019;22(1):1–13.
103. Bin Cai G, Chen SF, Liu L, Jiang J, Yao HB, Xu AW, et al. 1,3-Diamino-2-hydroxypropane-N, N, N', N'-tetraacetic acid stabilized amorphous calcium carbonate: Nucleation, transformation and crystal growth. *CrystEngComm.* 2010;12(1):234–41. doi:10.1039/B911426M.
104. Matei C, Berger D, Dumbrava A, Radu MD, Gheorghe E. Calcium carbonate as silver carrier in composite materials obtained in green seaweed extract with topical applications. *J Sol-Gel Sci Technol.* 2020;93(2):315–23. doi:10.1007/s10971-019-05145-6.
105. Jaman A, ABA MUN, Widyayanti OA. Synthesis of white mineral trioxide aggregate (WMTA) using silica from rice husk and calcium carbonate from limestone. *J Kim Sains Dan Apl.* 2023;26(2):64–9. doi:10.14710/jksa.26.2.64-69.
106. Ismail R, Fitriyana DF, Santosa YI, Nugroho S, Hakim AJ, Al Mulqi MS, et al. The potential use of green mussel (*Perna Viridis*) shells for synthetic calcium carbonate polymorphs in biomaterials. *J Cryst Growth.* 2021;572:1–8.
107. Sahana H, Khajuria DK, Razdan R, Mahapatra DR, Bhat MR, Suresh S, et al. Improvement in bone properties by using risedronate adsorbed hydroxyapatite novel nanoparticle based formulation in a rat model of osteoporosis. *J Biomed Nanotechnol.* 2013;9(2):193–201. doi:10.1166/jbn.2013.1482.
108. Gritsch L, Maqbool M, Mouriño V, Ciraldo FE, Cresswell M, Jackson PR, et al. Chitosan/hydroxyapatite composite bone tissue engineering scaffolds with dual and decoupled therapeutic delivery: Copper and strontium. *J Mater Chem B.* 2019;7(40):6109–24. doi:10.1039/C9TB00897G.
109. Quinaz T, Freire TF, Olmos A, Martins M, Ferreira FBN, de Moura MFSM, et al. The influence of hydroxyapatite crystals on the viscoelastic behavior of poly(vinyl alcohol) braid systems. *Biomimetics.* 2024;9(2):1–26.
110. Mohd Pu'ad NAS, Koshy P, Abdullah HZ, Idris MI, Lee TC. Syntheses of hydroxyapatite from natural sources. *Heliyon.* 2019;5(5):1–14.
111. Sari M, Yusuf Y. Synthesis and characterization of hydroxyapatite based on green mussel shells (*Perna viridis*) with the variation of stirring time using the precipitation method. *IOP Conf Ser Mater Sci Eng.* 2018;432(1):1–15.
112. Obada DO, Aliyu A, Kuta UM, Lisiyas A, Ogenyi VF, Aquatar MO, et al. Trends in the development of hydroxyapatite from natural sources for biomedical applications. *WIT Trans Ecol Environ.* 2022;257(2022):199–210.
113. Su Y, Li K, Wang J, Xie W, Zhu X, Wang C. Effect of the heating time on the preferred growth of hydroxyapatite crystal prepared by microwave-hydrothermal technique on the defective surface of sprayed coating. *Compos Part B Eng.* 2019;176:1–11.
114. Sun RX, Lv Y, Niu YR, Zhao XH, Cao DS, Tang J, et al. Physicochemical and biological properties of bovine-derived porous hydroxyapatite/collagen composite and its hydroxyapatite powders. *Ceram Int.* 2017;43(18):16792–28. doi:10.1016/j.ceramint.2017.09.075.
115. Mardziah CM, Ramesh S, Tan CY, Chandran H, Sidhu A, Krishnasamy S, et al. Zinc-substituted hydroxyapatite produced from calcium precursor derived from eggshells. *Ceram Int.* 2021;47(23):33010–9. doi:10.1016/j.ceramint.2021.08.201.